Non-Volatile Bipolar TiN/LaMnO3/Pt Memristors with Optimized Performance

Raquel Rodriguez-Lamas, Dolors Pla, Caroline Pirovano, Odette Chaix-Pluchery, Carlos Moncasi, Michel Boudard, Rose-Noëlle Vannier, Carmen Jiménez, Mónica Burriel

Materials Today Electronics 5 (2023) 100054

Contents lists available at ScienceDirect

Materials Today Electronics

journal homepage: www.elsevier.com/locate/mtelec

Full Length Article

Non-Volatile Bipolar TiN/$LaMnO_3$/Pt Memristors with Optimized Performance

Raquel Rodriguez-Lamas [a], Dolors Pla [a], Caroline Pirovano [b], Odette Chaix-Pluchery [a], Carlos Moncasi [a], Michel Boudard [a], Rose-Noëlle Vannier [b], Carmen Jiménez [a], Mónica Burriel [a,*]

[a] Univ. Grenoble Alpes, CNRS, Grenoble INP, LMGP, 38000, Grenoble, France
[b] Univ. Lille, CNRS, Centrale Lille, Univ. Artois, UMR 8181 – UCCS – Unité de Catalyse et Chimie du Solide, F-59000, Lille, France.

ARTICLE INFO

Keywords:
Resistive switching
valence change memories (VCMs)
manganites
memristive devices
metal organic chemical vapor deposition (MOCVD)

ABSTRACT

$LaMnO_{3+\delta}$ (LMO) perovskite is a very interesting candidate for Valence Change Memories due to its flexible stoichiometry, accommodated through the Mn^{+3}/Mn^{+4} equilibrium, at the origin of significant resistivity changes. Here, the successful combination of a LMO layer, with a top active TiN electrode and a bottom inert Pt electrode, is presented. The manganite layer is integrated on silicon-based substrates in the form of a polycrystalline film. By comparing the memristive behavior of these TiN/LMO/Pt devices with Au/LMO/Pt devices prepared on the same film, the essential role of the active oxygen electrode is put in evidence. TiN/LMO/Pt memristive devices show optimized performance, operating in both sweep and pulse mode, with the capability of cycling more than a hundred times and showing good retention. Furthermore, a simple phenomenological model describing the memristive behavior of the devices is also presented.

1. Introduction

The evolution of information storage requires faster devices with higher storage density and lower power consumption. These requirements become fundamental when the number of devices equipped with a memory cell multiply exponentially, which is expected from the development of the Internet of Things-related technologies, neuromorphic computing [1], and the in memory computing paradigm [2]. Memristive devices emerged as promising candidates for such non-volatile memory applications. They are based on the reversible phenomena occurring in two terminal circuit elements, which present resistance changes under the effect of electrical stimuli (applied electric field) in a non-volatile manner, i.e. the different resistance states (two or more) are preserved in absence of electric field [1,3]. This phenomenon is known as resistive switching (RS).

Most memristive devices, capable of retaining an internal resistance state which is determined by the applied voltage (and current) history [4], require an activation protocol. Usually, it consists of an "electroforming" process, by the application of a voltage much higher than its operation range, which typically leads to the creation of a conducting filament [5]. However, its stochastic nature leads to limitations in device-to-device and cycle-to-cycle reproducibility and entails the risk of a dielectric breakdown [6,7], leading to device failure. Breakdown is typically produced by avalanche currents created by self-accelerated thermal effects which lead to irreversible atomic rearrangement [8]. As alternative activation protocol, a gradual separation of resistance states can be obtained upon continuous I-V cycling. This process, defined by the community as "initialization" [9], is the one targeted in our work to avoid the risk of device failure.

Valence change memories (VCM), based on redox processes [10], present bipolar resistive switching based on the drift of oxygen vacancies in an oxide matrix [11,12] and the concomitant changes in oxidation state of the cation sublattice. In recent years, particular attention has been paid to perovskites as active materials for these two terminal memristive devices, [13,14] since the possibility to vary the oxygen non-stoichiometry provides a solid base for these redox mechanisms. In this sense, the $LaMnO_{3+\delta}$ manganite is a suitable candidate for VCMs since its flexible stoichiometry is accommodated by a valence change in Mn through an equilibrium Mn^{+3}/Mn^{+4}.

In general, VCM switching phenomena are classified according to

* Corresponding author.
E-mail addresses: raquel@rodriguezlamas.com (R. Rodriguez-Lamas), alolalp@gmail.com (D. Pla), caroline.pirovano@univ-lille.fr (C. Pirovano), odette.chaix@grenoble-inp.fr (O. Chaix-Pluchery), carlosmoncasi.l@gmail.com (C. Moncasi), michel.boudard@grenoble-inp.fr (M. Boudard), rose-noelle.vannier@centralelille.fr (R.-N. Vannier), carmen.jimenez@grenoble-inp.fr (C. Jiménez), monica.burriel@grenoble-inp.fr (M. Burriel).

https://doi.org/10.1016/j.mtelec.2023.100054
Received 12 October 2022; Received in revised form 13 July 2023; Accepted 27 July 2023
Available online 28 July 2023

their localization, with three main scenarios: i) interfacial RS, when a redistribution in oxygen ions (or oxygen vacancies, $V_O^{\cdot\cdot}$) occurs locally over the whole electrode area, ii) volumetric RS, with a change in the whole oxide, and iii) filamentary RS, with a local change across the matrix in the form of one or more filaments. There are also mixed scenarios, generally dominated by one of the three cases described. In general, interfacial switching, which depends on Schottky barrier modulation, narrowing of a tunneling barrier, or others, tends to be associated with gradual changes in resistance [15–17] while filamentary switching is more frequently related to abrupt changes in resistance [18–20]. Finally, volumetric switching is usually associated to phase changes [21] in the oxide matrix, or to metal-insulator transitions [22].

In the case of perovskites, as exemplified by the canonical $SrTiO_3$ (STO), both types of switching can occur [14]. Both the formation of a Schottky barrier between the electrode and the oxide matrix surface [23–25], leading to interfacial RS, and the formation of such barrier between the electrode and conducting filaments embedded in the oxide matrix [26,27] have been observed.

Some studies on vertical devices integrating polycrystalline STO [28,29] on top of a platinum [28] or a titanium [29] bottom electrode have shown remarkable results such as: low current, down to 1 mA, operating voltages in the range of 1-3 V for I-V cycle operation and at least 100 cycles endurance. To be operated, these cells required electroforming, in the voltage range of 1 to 8 V. Mott transition based devices, such as sputtered $La_2Ti_2O_{7-x}$ have shown electroforming-free RS when operating in lower voltage ranges, namely up to 2.2 V [30]. Different systems, integrating manganite films such as $La_{1/3}Ca_{2/3}MnO_3$ (LCMO), combined with a bottom electrode of n-type Si [31], have also been reported. According to literature, the use of polycrystalline thin oxide films, would be advantageous, given the potential of grain boundaries to act as fast diffusion channels for $V_O^{\cdot\cdot}$ and other defects [32], related to the easy formation of oxygen conducting paths [33].

As for undoped $LaMnO_{3+\delta}$, first studies on epitaxial films provided evidence of the fundamental role of oxygen vacancies in the RS response [34]. Later on, the first proof of concept of polycrystalline LMO-based on Au/LMO/Pt vertical memristive devices [35] was reported, followed by the study of the microscopic mechanisms of local interfacial RS in LMO using conductive Atomic Force Microscopy (c-AFM) [36] combined with spectroscopic techniques (X-ray photoemission electron microscopy (XPEEM) and Raman spectroscopy). The study concluded that under an electric field, oxygen was driven out and back in from the sub-surface to the surface, reducing and oxidizing locally the Mn in the LMO film. These processes occurred without a "real" top electrode, but using an AFM tip. Nevertheless, it was only possible to cycle the system a limited number of times, probably due to an oxygen release to the atmosphere under vacuum conditions.

These studies were complemented by the hard X ray photoelectron spectroscopy (HAXPES) on M/LMO/Pt where M=Pd, Au [37] and on TiN/LMO/Pt [38] vertical devices, using adapted vertical heterostructures designed for *operando* measurements. The TiN-electrode heterostructures showed the best performance with increased device cyclability and a HRS/LRS ratio in the order of 10^4. The HAXPES spectra of Ti 1s and O 1s demonstrated the occurrence of a redox reaction at the TiN/LMO interface triggered by the oxygen drift, i.e. a partial oxidation of the TiN electrode and reduction of the LMO surface during RESET, followed by the partial reverse reactions during SET. These results revealed the role of TiN as an oxygen reservoir (with a variable amount of oxygen in the form of titanium oxynitride, TiO_xN_y). While the use of TiN is fundamental, LMO acts as oxygen source, accommodating the oxygen stoichiometry changes through valence changes of the Mn cation, which globally leads to resistance changes. Other studies in the literature also describe the exchange of oxygen between TiN_yO_x and the oxide layer, such as HfO_2 [39], a $HfO_2/TiO_2/HfO_2$ trilayer [40] or $Pr_{1-x}Ca_xMnO_3$ [41]. In particular, the *in-situ* TEM study on TiN/PCMO/Pt devices demonstrated that the redox electrochemical reactions taking place at the TiN/PCMO interface are facilitated by electric field-driven drift of both oxygen and titanium ions [41]. The TiO_xN_y interface layer governs the reaction kinetics and determines the critical field for the onset of the switching ($\sim 10^6$ V•cm^{-1}). This onset value is in good agreement with the nonlinear ionic drift model proposed by the authors as switching mechanism. Finally, it should also be noted that high endurance (of more than 10000 cycles) and low operational voltage (±1 V) were recently reported for LMO-based memristive devices using an electrode combination of Ag and ITO [42].

In this work, we aim to study and optimize for the first time the device operation and RS performance of M/LMO/Pt heterostructures, using TiN as oxygen reservoir top electrode, enabling a robust memory performance. The fabrication of M/ polycrystalline LMO/Pt devices with both Au and TiN electrodes on the same sample allows for direct comparison of the influence of the top electrode in the RS performance. Contrary to TiN, the noble metal (Au) devices, characterized by an ohmic contact with LMO [43,44], did not present non-volatile memristive behavior, while the bipolar RS was confirmed for the TiN devices. The results obtained provide new insights on the promising use of this polycrystalline LMO combined with TiN, as oxidizable electrode, for memristive device applications.

2. Film growth and device preparation

$LaMnO_{3+\delta}$ (LMO) thin film growth was performed in a pulsed injection metal-organic chemical vapor deposition (PI-MOCVD) JIPELEC reactor, extensively described in our previous article. [35] Commercial tris(2,2,6,6-tetramethyl-3,5-heptanedionato) lanthanum (III) [La(thd)$_3$] and tris(2,2,6,6-tetramethyl-3,5-heptanedionato) manganese (III) [Mn(thd)$_3$], provided by Strem chemicals, were used as metalorganic precursors, and m-xylene (1,3-dimethylbenzene) from Alfa Aesar was the solvent of choice. The precursor solution was prepared with a total concentration of 0.0225 M and a La/Mn ratio of 2. The injection of the precursor in the evaporator was performed at a 2.5 Hz frequency, using a 2 ms electrovalve opening time, leading to a solution feeding rate of 0.35 ml/min. The reactor chamber temperature was set to 675 °C and a 50%/50% mixture of O_2 and Ar with a total pressure of 5 Torr was set during the growth and cool down of the sample. In this work, 1 × 1 cm^2 chips cut from the commercial Pt (150 nm)/TiO_2 (50 nm) /SiO_2 (500 nm)/Si (111) wafer from Vin Karola Instruments were used as substrates. A hard mask was used to fix the substrate to the substrate holder and to leave a region of Pt uncovered, to be electrically contacted as bottom electrode. For in plane conductivity measurements, performed in a Pro-4 four-point probe station coupled to a Keithley 2400 source meter, the deposition was also performed on Si_3N_4 (300 nm) /SiO_2 (200 nm) /Si (001) substrates.

The surface morphology was studied through scanning electron microscopy (SEM) in a Quanta250 environmental SEM FEG from FEI in high vacuum mode, using beam energies in the range of 5 - 10 kV. The cationic film composition was originally analyzed by semi quantitative energy-dispersive X-ray analysis (EDX) using an Oxford Inca Energy detector coupled to the SEM and using a Cu film as calibration reference. The thin film composition was then corroborated by Rutherford backscattering spectrometry (RBS) performed at the Centro de Micro-Análisis de Materiales - Universidad Autónoma de Madrid (Spain) using the 5 MeV tandetron accelerator. RBS was performed with a 2 MeV He^+ beam by using silicon surface barrier detectors placed at a scattering angle of 170°. The analysis of O and C was performed by a $^4He^+$ ion beam at oxygen and carbon resonant energies of 3.035 MeV and 4 MeV respectively [45]. Each data set was obtained by depositing a charge of 12 μC. All spectra were simulated using the SIMNRA code [46] to obtain the element in-depth composition.

The crystal structure of the film was analyzed through the combination of grazing incidence X-ray diffraction (GIXRD) performed in a 5-circle Rigaku Smartlab diffractometer and Raman spectroscopy using a Jobin Yvon/Horiba Labram spectrometer equipped with a liquid nitrogen-cooled CCD detector. The spectra were acquired in the micro-

Raman mode in a backscattering geometry using a green laser (λ = 514.5 nm). The silicon spectrum at ambient temperature was measured as reference to calibrate the spectra. The topographic images and the root mean square (rms) roughness were obtained by atomic force microscopy (AFM) in tapping mode in an AFM Digital Instruments Dimensions 3100 (Veeco) through the Nanoscope Interface with a resonance frequency in the range of 270 ± 10 kHz. AFM data treatment was performed in Gwyddion software.

Time of flight secondary ion mass spectroscopy (ToF-SIMS) analysis of the composition in the three dimensions of the thin film was performed. A ToF-SIMS V instrument (ION-TOF GmbH Germany) equipped with a Bi liquid metal ion gun (LMIG) for analysis and a cesium (Cs^+) gun for sputtering was used for the oxygen isotope analyses. Negative secondary ions were collected and the data were obtained by 6 pulses burst mode operation, applying Poisson correction. Charge effects were compensated by means of a 20 eV pulsed electron flood gun. A 300 × 300 μm^2 surface area was sputtered with the Cs^+ ion beam (1 keV, 85 nA) before analysis with the Bi^{3+} primary ion beam (25 keV, 0.25 pA) rastered over a 50 × 50 μm^2 surface area.

The device fabrication was processed in the PTA clean-room facilities to obtain several arrays of TiN and Au top electrodes on the same sample, as described in **Figure S1**. Each device consists of a top metal electrode (M = TiN, Au) of 100 nm, the continuous LMO film (75 nm) and the bottom Pt electrode (150 nm). The fabrication flow combined laser lithography using a Heidelberg instruments μPG 101 system, metal evaporation and lift off processes. An array of 4 columns of electrodes with different sizes, namely 200 × 200 μm^2, 150 × 150 μm^2, 50 × 50 μm^2 and 100 × 100 μm^2 (from the exposed Pt electrode and towards the opposite sample edge) distributed in 14 rows, was designed. The sputtering of a 100 nm thick TiN layer was performed through physical vapor deposition (PVD) in a CT100 Alliance concept. The electrode array was cloned to obtain a second identical pattern of 56 Au electrodes (100 nm thick), which were evaporated in a MEB 550 Plassys evaporator.

The electrical characteristics were obtained under ambient conditions within a Faraday cage in a Karl Suss probe station with microprobe manipulators using a B1500 Agilent semiconductor parameter analyzer. The Pt electrode was grounded and the voltage was applied onto the top electrode. The initial resistance state (IRS) of the memristive devices was evaluated by measuring the current at 100 mV. The few devices that presented a very low resistance value (IRS<9 Ω), which could indicate short-circuits or leakage, were discarded. The results presented in this work correspond to 33 TiN/LMO/Pt memristive devices which IRS was in a range of 9-300 Ω. In addition, three main types of measurements were performed in this system: i) I-V sweeps in both polarities using a rate of 0.005 V/step. ii) I-V pulsed measurements alternating write and read pulses. iii) Retention measurements through the application of a read voltage of 100 mV every 60 s. The standard read voltage used for all measurement was of 100 mV unless otherwise specified.

3. Morpho-structural characterization and composition analysis

$LaMnO_{3+\delta}$ thin films were grown at a 675°C by the injection of 6000 pulses for a thickness of 75 nm. The same Ar/O_2 mixture used during thin film growth was kept during the cooling to obtain a film with a mixed orthorhombic/rhombohedral structure. [35] The La/Mn cationic ratio was estimated to be 1.06 ± 0.1 by Rutherford backscattering spectrometry (RBS). The obtained spectra and simulation fitting are presented in **Figure S2** in the electronic supplementary information (ESI). The crystal structure of this film was found to be a mixture between orthorhombic and rhombohedral phases, as confirmed by X-ray diffraction and Raman spectroscopy (Fig. 1). The LMO film crystal structure was validated through GIXRD and presented in Fig. 1**a**. The diffraction peaks correspond to the superposition of the peaks of the LMO perovskite (polycrystalline) and of the Pt from the substrate, without the presence of any impurity phase. The comparison of the LMO diffraction pattern with the ICDD reference patterns for the orthorhombic (Pnma) and rhombohedral (R-3c) LMO structures, which main peaks overlap, confirms the presence of the LMO perovskite phase, with a mixture of both structures. Several Raman spectra were acquired in different regions of the sample, giving very similar results. The representative Raman spectrum shown in Fig. 1b points towards a mixture of orthorhombic and rhombohedral phases of LMO. A purely orthorhombic structure, as presented by Iliev et. al. [47], would present a sharp mode at 611 cm^{-1} (B_{2g}), as well as broader modes at 493 cm^{-1} (A_g) and 284 cm^{-1} (A_g). However, the broadness of the mode close to 611 cm^{-1} and the apparition of an additional mode around 650 cm^{-1} together with another one at ~500 cm^{-1}, can be explained by the existence of Jahn-Teller (J-T) distortion modes corresponding to rhombohedral LMO, as reported by Iliev. Thus, the Raman spectra confirm the co-existence of orthorhombic and rhombohedral phases, as demonstrated in our previous work. [35]

Optimized memristive devices must show flat surfaces, the absence of pinholes, and a homogeneous chemical composition in the whole device area. Fig. 2**a** and 2**b** show a SEM secondary electron and an AFM topography image of the top surface of the polycrystalline sample. The film exhibits small homogeneous grains, with a 20 ± 7 nm diameter and a film roughness (rms) of 4.0 ± 0.5 nm, confirming the suitability of the LMO thin films for proof of concept device fabrication. The four representative profiles extracted from AFM maps shown in Fig. 2**c** illustrate the surface roughness. In future work, when device miniaturization is tackled, the surface roughness should be reduced to meet

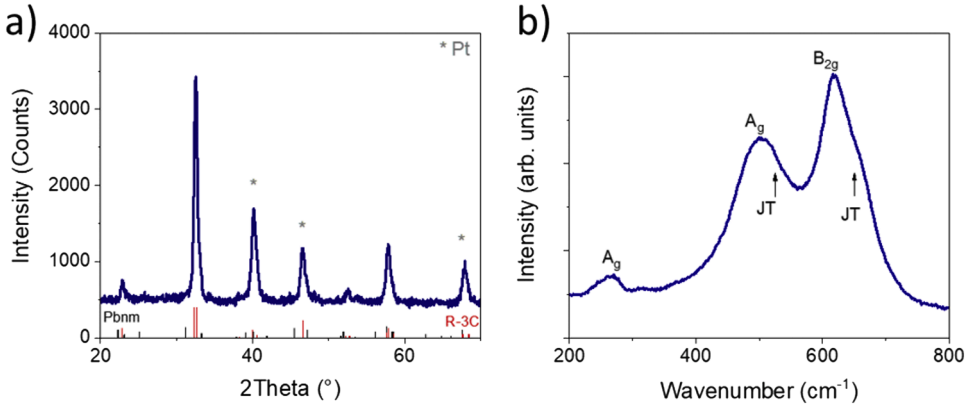

Fig. 1. a) GIXRD pattern of the LMO film and ICDD reference patterns n° 01-087-2015 and 04-007-6350 for the orthorhombic (Pnma) and rhombohedral (R-3c) LMO structures, respectively. b) Raman spectrum acquired at the center of the LMO thin film sample. Symmetry assignments (A_g and B_{2g} modes) correspond to the orthorhombic structure, while the Jahn-Teller (J-T) modes correspond to the rhombohedral structure.

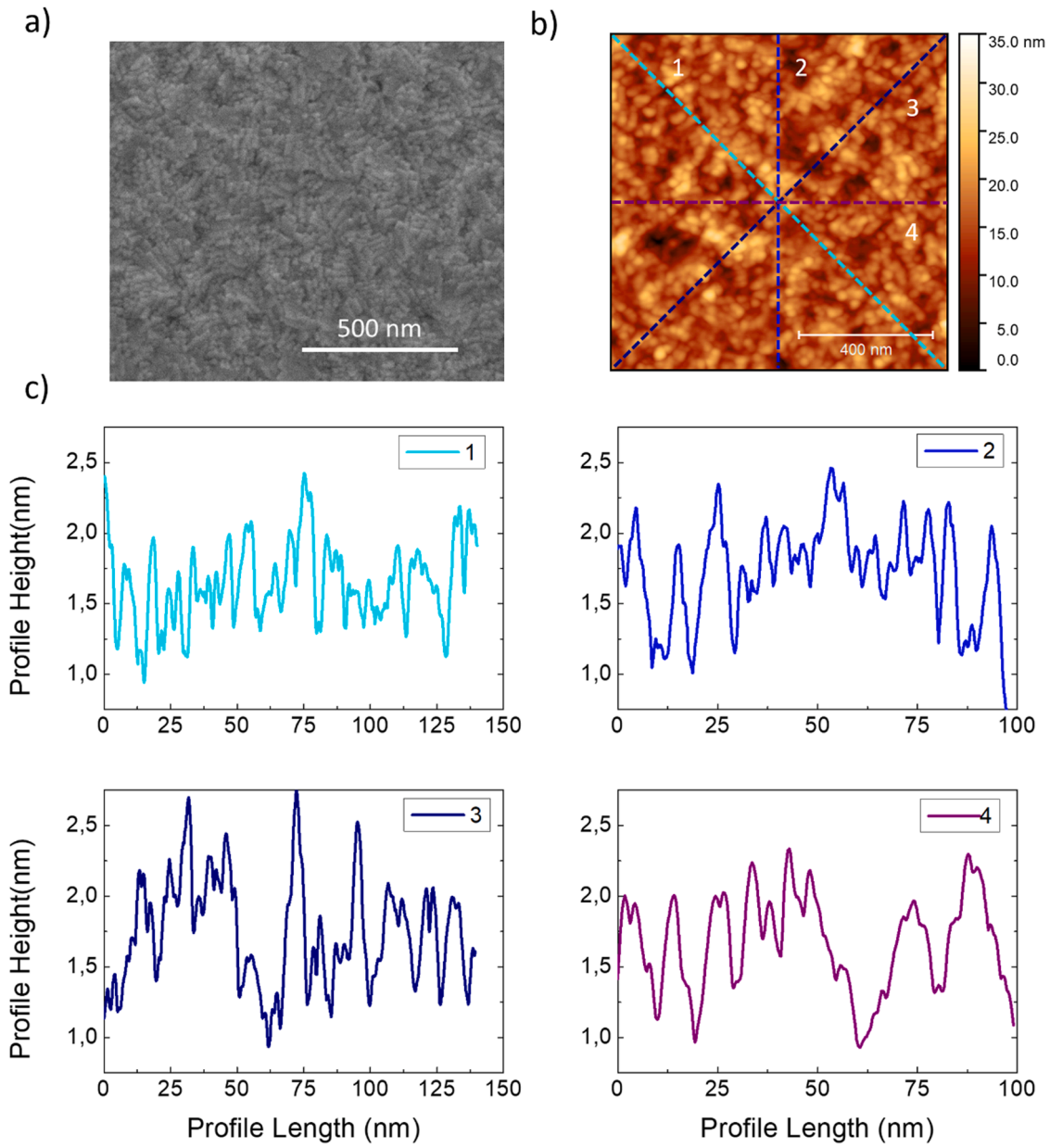

Fig. 2. a) Surface morphology imaged by SEM as secondary electron image. b) AFM topography of the film surface, including c) four representative profiles across the image to illustrate the surface roughness of the polycrystalline film (1-4)

microelectronics fabrication standards.

In addition, the composition homogeneity was verified across the film (z direction) using ToF-SIMS. Fig. 3**a** shows the negative ions depth profile across the LMO film. After the first nanometers of the top surface, the La and Mn concentration is almost constant. However, a small incorporation of oxygen into the Pt bottom electrode is observed. The Pt^- ion intensity raise at the Pt/oxide interphase (Fig. 3a) is probably due to an increase in the SIMS relative sensitivity factor due to a matrix effect in presence of O^-, as previously observed for other layered interphases. [48,49] The depth profile in Fig. 3a, together with the 3D views of the analyzed volume for each ion species (Fig. 3**b** and 3**d**) confirm flat interfaces and the absence of pinholes in the film. The top surface observations of the different ions (Fig. 3**c**) prove the homogeneous spatial distribution of all species. The mapped region corresponds to an area of 50 × 50 μm^2, comparable to the smallest devices fabricated. The 3D images of O^- (Fig. 3b), MnO^-, LaO^- and Pt^- (Fig. 3**d**) show a uniform distribution of all ions of interest and support that no intermixing is given across the heterostructure, and no percolation of Pt into the LMO film.

4. Device performance

The conductivity of LMO varies with the crystal structure, while orthorhombic phase has been reported as insulating phase, rhombohedral LMO shows better conductivity. The resistivity measured for LMO films grown on $Si_3N_4/SiO_2/Si$ substrates under the same deposition conditions is 16 ± 4 Ω•cm, in good agreement with literature values [50] given the mixed orthorhombic/rhombohedral character of the sample. The series resistance contribution for the LMO film is thus in the range of $2•10^{-1}$ - $1•10^{1}$ Ω for the vertical devices, depending on their size.

The devices were subjected to an initialization process consisting of the iteration of I-V sweep "cycles" ($0 \rightarrow V_{max} \rightarrow 0 \rightarrow -V_{max} \rightarrow 0$), as shown in Fig. 4**a** for a 50 × 50 μm^2 device. For optimal operation V_{max} was varied between 1 and 2 V, according to the maximum achievable high resistance state (HRS)/ low resistance state (LRS) ratio, without

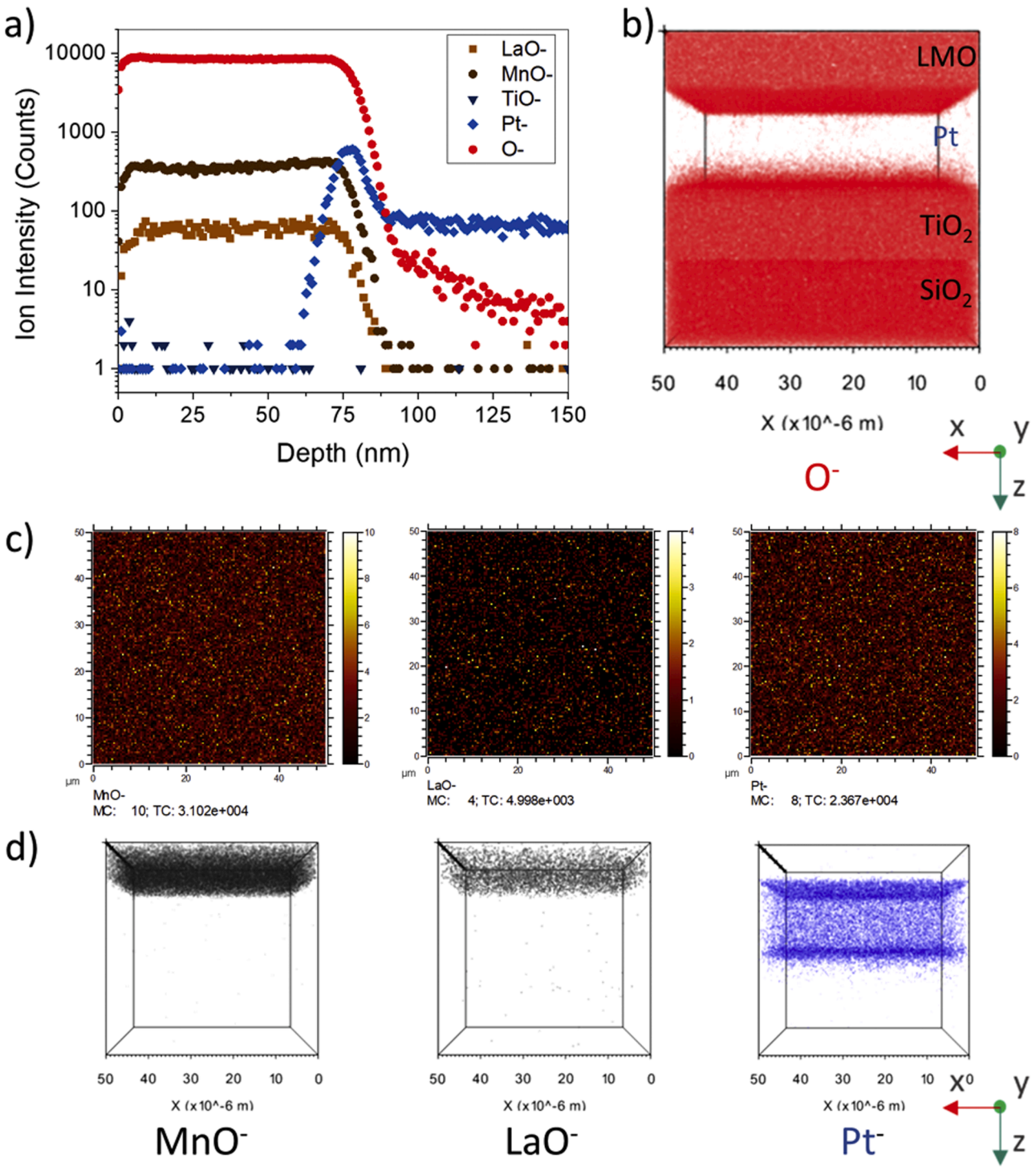

Fig. 3. a) O^-, LaO^-, MnO^-, TiO^- and Pt^- ToF-SIMS negative ion depth profiles, measured for an LMO film grown on $Pt/TiO_2/SiO_2/Si$. 3D analysis of the ToF-SIMS data: b) 3D representation of oxygen ions (red); and c) top view and d) 3D representation of MnO^-, LaO^- (both in grey) and Pt^- (blue) ions in the whole analyzed volume.

overcoming the current compliance limits. An example of current overshoot due to high current limits is provided in **Figure S3**. During the first 10 cycles, each cycle leads to a slightly larger separation of the HRS and LRS values, until a maximum is reached. This initialization process has the advantage of avoiding current spikes known to occur during conventional electroforming. 40 mA and 60 mA were used as current compliance for the positive and negative polarities, respectively. After initialization, the devices can operate by I-V sweeps, cycling in counter clock wise (CCW) sense. In agreement with our previous work [36], from the I-V shape studied for devices of all sizes we found good agreement with a Space Charge Limited Conduction (SCLC) mechanism (slopes in log I-log V representation presented in **Figure S4**).

The devices were cycled continuously, up to 100 times in some cases, with very low cycle to cycle variability and a very stable HRS/LRS ratio. The cumulative probability over more than 30 cycles for three devices of three different sizes is presented in **Figure S5**, showing a good separation between the HRS and LRS for all devices, and the relatively small variability for each state.

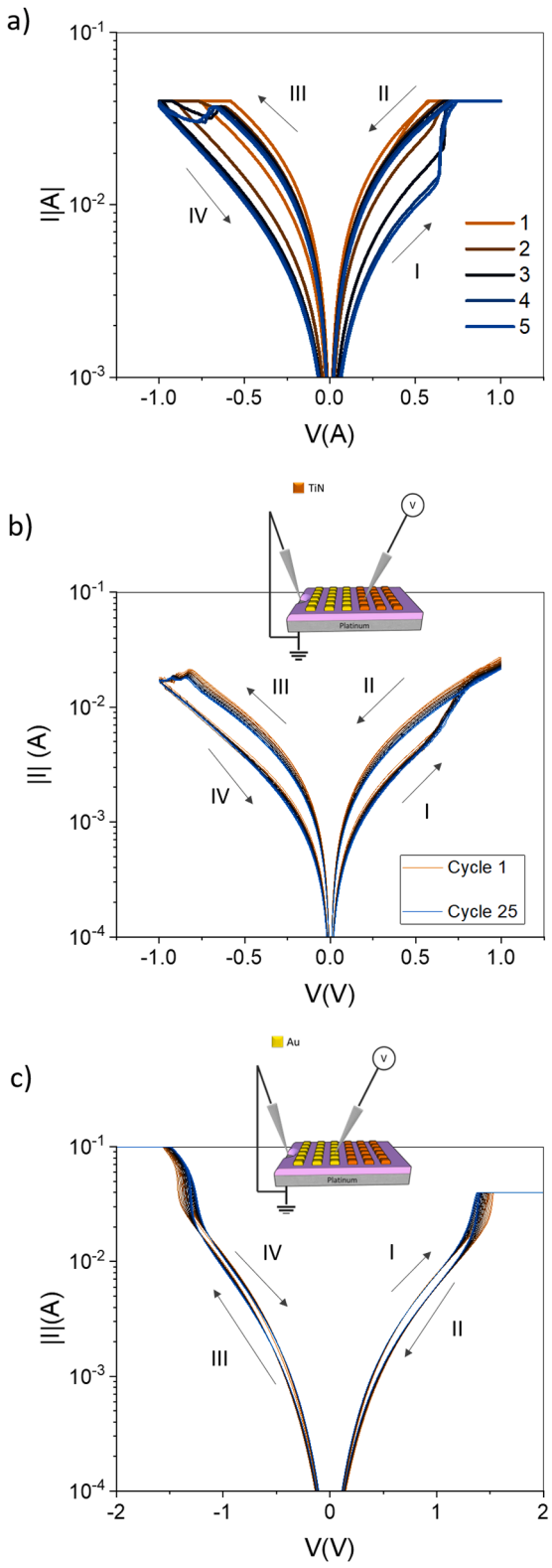

Fig. 4. a) Cycle by cycle 'initialization' protocol in a 50 × 50 μm^2 TiN/LMO/Pt device. The current evolution (in logarithmic scale) with voltage is represented for the first 4 cycles, where the maximum separation HRS/LRS is obtained for cycle 4. And comparison of I-V sweeps between 100 × 100 μm^2 devices with different top electrodes. b) 25 consecutive I-V sweep cycles for a TiN/LMO/Pt device. Current compliance is not reached. c) 15 consecutive I-V sweep cycles for an Au/LMO/Pt device. Current compliance is set to Icc= -100 mA in the negative polarity and 40 mA in positive.

The best combination between high HRS/LRS ratio and LRS variability led to an HRS/LRS ratio of 3.3 ± 0.2, calculated over 25 cycles in the optimized operation regime for a V_{max} value of 1 V (Fig. 4**b**). Plots showing the evolution of the read HRS and LRS states during consecutive cycling of two different devices of 100 × 100 μm^2 have been included in **Figure S6** in ESI. In addition, for these devices, by increasing the V_{max} and Icc values respectively, the HRS/LRS ratio could be increased. A series of five I-V cycles with HRS/LRS ≈ 10 is represented in **Figure S7**. Nevertheless, both the variability of the resistance states (HRS, LRS) and the risk of device failure increased, reducing the number of consecutive stable cycles.

To simulate real device operation conditions the TiN/LMO/Pt memristive devices were also tested in voltage pulse operation mode. By applying a 0.1 V/0.1 s read pulse after each write pulse, two stable resistance states are clearly observed for a wide voltage range (Fig. 5**a**). Fig. 5**b** shows the pulse scheme used for the resistance hysteresis switching loop (RHSL) measurements in which write and read pulses are alternated.

Furthermore, another 50 × 50 μm^2 device was also reproducibly operated by a series of alternate positive and negative pulses each followed by a read pulse. Combining different pulse height and width, we studied the variations on the switching window (**Figure S8** ESI). Through the variation of these parameters, different levels of resistance can be read, this would hint towards a potential multilevel character. In Fig. 6**a** and 6**d** the conditions leading to the largest obtained window were adopted. These results provide the proof of concept for operation of memory cells based on TiN/LMO/Pt heterostructures.

The retention of the resistance states was also tested. As standard protocol the devices were left in LRS, which was always preserved for weeks, with variations lower than 0.1%, confirming their stability over time. After the pulsed measurements, the retention of the HRS of a device was measured intermittently for 14 hours (one measurement every 60 s), showing a low variation of 1.7%, proving good stability for at least this time (Fig. 6**b** and 6**d**). The retention measurement was followed by an additional negative and a positive pulse (Fig. 6**c** and 6**d**), proving that after the retention period the device still operates in the same reproducible manner.

To evaluate the type of switching, i.e. interfacial, volumetric or filamentary, devices of four different top electrode sizes were used. The variation of the resistance states with the electrode size (Fig. 5**c**) shows no area dependence for the small electrodes; and only the largest electrodes (200 × 200 μm^2) resistance states show a value lower than the average. In this figure, only the median values of the HRS and LRS for the devices cycled more than ten times are included. Larger statistics including all successfully initialized devices are shown in **Figure S9**. Furthermore, a study of the variability of the set and reset voltage for the devices of different sizes can be found in **Figure S10** [51], where the set voltage values where found between 0.5 V and 1.2 V and the reset voltages between -0.7 V and -1.2 V. One additional strategy to study the filamentary and non-filamentary contribution relied on a first approach to calculate the device series resistance for devices of different sizes. An example of the methodology, as described by Maldonado et.al. [52] is presented in ESI **Figure S11**. The series resistance has been extracted for several devices of all sizes (ESI **Figure S12**). While the lack of area dependence, form Figure S12, agrees with a filamentary behaviour and the fit can be performed to the linear region after V_{SET}, the deviation shown by the non-linear contribution in Figure S11b, points towards a non- filamentary contribution. The series resistance obtained for the TiN/LMO/Pt stacks is in the same order of magnitude as that extracted by Meunier et. al. in previous studies of similar devices by a different method [38]. These results hint towards a switching mechanism dominated by the filamentary behavior, and modulated by the interfacial phenomena revealed in our previous fundamental study, in which an exchange of oxygen between TiN and LMO was observed. [38]

To confirm the role of TiN as active electrode, these devices were compared with others prepared using Au (noble metal) top electrodes on

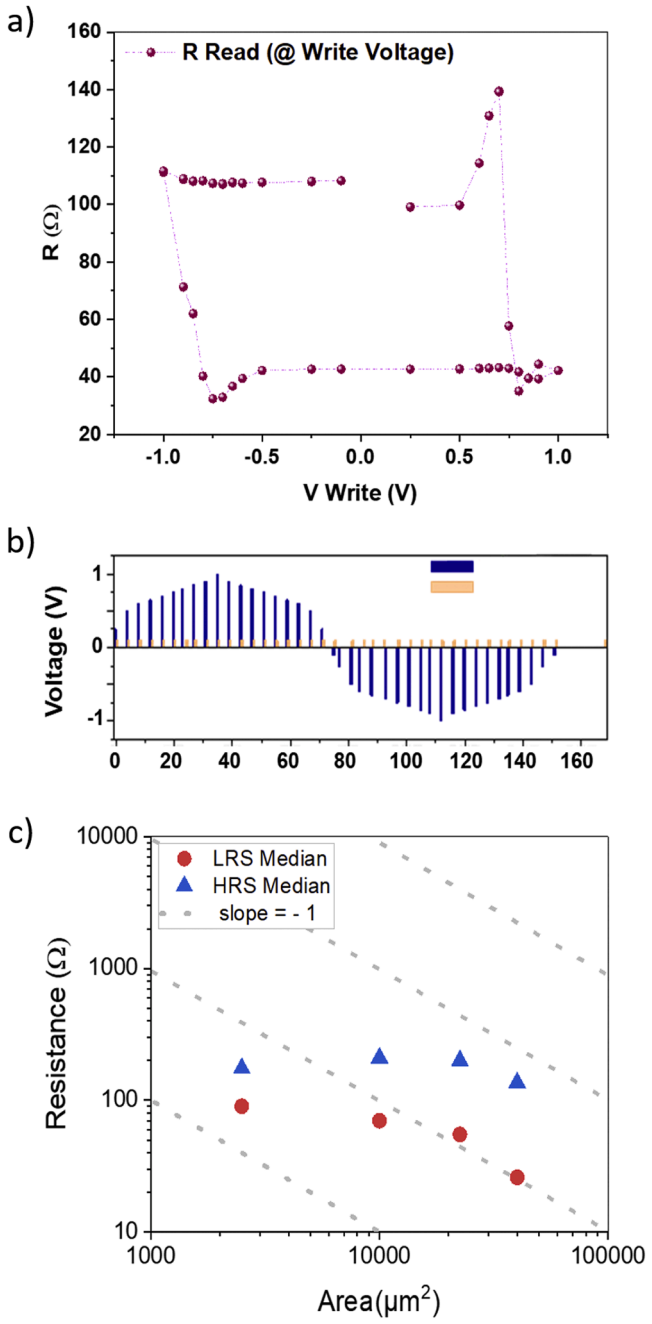

Fig. 5. a) Voltage pulse operation of a 50 × 50 μm^2 device. Read resistance values extracted from read pulses, showing two stable states in absence of field. b) Corresponding train of write and read consecutive pulses in the hysteresis loop reproducing an I-V sweep curve. c) LRS and HRS resistance dependence with the top electrode size. For each size, the plotted value corresponds to the median value of a total of 3 to 5 measured devices corresponding to the most reproducible RS response. These devices were selected following two criteria: they must have been tested with consecutive I-V sweeps a minimum of 10 consecutive times and they must have comparable history.

the same LMO thin film sample. Fig. 4**c** shows 15 consecutive I-V cycles for a 100 × 100 μm^2 Au electrode device, after a similar initialization protocol. It is important to notice that here the RS takes place clockwise (CW). I–V characteristics with opposite switching sense have been previously related to oxygen exchange at the Pt/oxide interface [53]. As the switching mechanism is based on oxygen vacancy migration and the voltage is being applied to the Au top electrode, which has lower oxygen affinity than Pt [54], in this case the main RS phenomena should occur at the LMO/Pt bottom interface. Although the initial resistance of the Au devices (20-160 Ω) is in the same range as that of the TiN devices (9-300 Ω), during the first cycle the resistance of the Au/LMO/Pt device increases up to 1.4 kΩ. This increase can be explained by the loss of oxygen from the LMO layer, possibly drifting into the Pt, which would provoke a reduction of the Mn cations and a decrease in hole conduction. This voltage-mediated oxygen drift was previously observed in c-AFM experiments carried out on the same material. [36,37] As shown in Fig. 2d, in the Au/LMO/Pt configuration only a small separation between HRS and LRS with an HRS/LRS ratio of 1.3 can be reached, with no retention over time, i.e. the Au-based devices are volatile. The small separation of states, and their lack of retention highlight the importance of the TiN electrode to obtain a non-volatile memristive response.

Taking into consideration the switching protocols and characteristics of the LMO polycrystalline memristive devices presented here, together with the results from our previous fundamental studies [36,38], a phenomenological model is proposed, as shown in Fig. 7. The gradual current-voltage characteristics of the devices activated through an initialization (Fig. 4a) with no abrupt jumps in resistance (Fig. 4b), are in good agreement with the relevance of the interfacial contribution brought to light in [38]. In addition, the systematic study performed for devices of different sizes hints towards a more intricate mechanism involving a mixed interfacial/filamentary behavior, as indicated by the absence of a clear scaling of HRS and LRS in Fig. 5c. During the initialization of the TiN/LMO/Pt devices, the interfacial LMO would be depleted from oxygen leading to a $LaMnO_{3+\delta'}$ ($\delta' < \delta$) region, with the TiN electrode acting as oxygen reservoir by the formation of TiO_xN_y. The existence of such oxygen depleted zones, and the exchange of oxygen with an active electrode is in good agreement with previous studies on manganites [55]. Considering the influence of the oxygen stoichiometry of the $LaMnO_{3+\delta}$ films on its electrical properties, the conductivity of LMO, a p-type conductor, increases with δ [56], and thus the oxygen-depleted LMO region is expected to have a larger resistivity. Besides, the TiO_xN_y layer will also contribute as a series resistance. Overall, both series resistances lead to a larger device resistance for the initialized device. Next, by applying a positive bias to the top electrode oxygen would drift forming conducting $LaMnO_{3+\delta}$ filaments through the oxygen-depleted LMO, connecting the low resistivity $LaMnO_{3+\delta}$ region to the TiN electrode, and leading to the change from HRS to LRS (see Fig. 4). When a negative polarity is applied, the filaments in the $LaMnO_{3+\delta}$ would disconnect from the top electrode, leading back to the HRS.

The present work is in good agreement with our previous observations and offers a broad statistical electrical characterization analysis (initial resistance state, I-V sweeps, pulses, electrode-size dependence, cyclability and retention) of the memristive behavior of LMO-based devices built with two different top electrodes. In the promising TiN/LMO/Pt system, the ability of LMO and TiN to alternatively exchange oxygen depending on the polarity sign is the base of the successful coupling which leads to two distinguishable and reproducible HRS and LRS states. Using TiN as top electrode, as opposed to Au, leads to higher HRS/LRS ratios and improves the endurance of the devices thanks to the incorporation and exchange of oxygen with the electrode, which acts as a reservoir preventing the degradation of the electrode/oxide interface and improving the device lifetime. Nevertheless, to meet the requirements of the application in the future the device resistance should be increased. This can be potentially achieved by: i) decreasing the oxygen content of LMO and changing the structure to an orthorhombic one (e.g. varying the deposition conditions) [35]; ii) by changing the microstructure to reduce the number of grain boundaries and/or iii) by adding interlayers of a material such as yttria-stabilized-zirconia, as successfully proven in the literature for PCMO [57]. Ideally, to meet the industrial standards, the devices should reach 0.1 μm^2 area, switching times of 10 ns, endurances of up to 10^{15} cycles and larger than 10 years retention times. However, as recently reported by Lanza et. al. [58] there is still a large gap between academia and industry in the field of

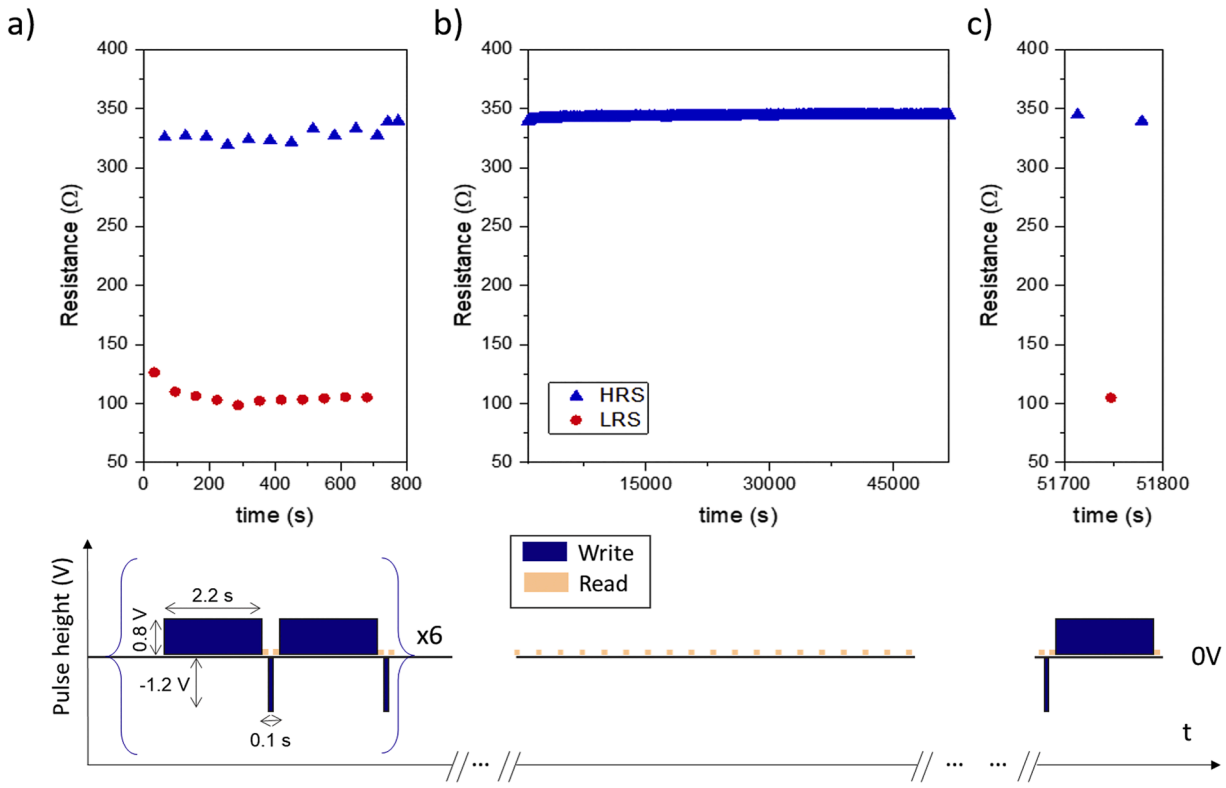

Fig. 6. a) Pulsed measurements, read resistance for HRS and LRS followed by b) retention measurement of HRS every 60 s during 14 h and c) a last set of read HRS and LRS after one last pulsed cycle. The corresponding trains of pulses alternating write pulses of 0.8 V heigth and 2.2 s width, read pulses of 0.1 V heigth and 100 ms, and write pulses of -1.2 V heigth and 0.1 s width. The retention was read with 0.1 V (0.1 s) pulses every 60 s and, last, a train of pulses using the same parameters as before verified that the states remained unchanged.

resistive switching, gap which should be narrowed in the future by taking into consideration the industrial requirements.

5. Conclusions

Homogeneous polycrystalline $LaMnO_{3+\delta}$ films deposited on platinized silicon, consisting in a mixture of rhombohedral and orthorhombic phases were used to construct memristive devices, which were fabricated in vertical configuration with TiN and Au top electrodes. The initialization protocol consisted of alternative voltage sweeps in positive and negative polarities, allowing the devices activation and leading to a clear separation of LRS and HRS states for the TiN/LMO/Pt devices. This protocol reduces the risk of breakdown compared to the typical electroforming. The devices were proved to cycle in CCW behavior for at least 100 times with low cycle to cycle variability and HRS/LRS ratios of 3.3 ± 0.2. The retention in HRS was of at least 14 h, and stable for the LRS. Furthermore, memristive behavior was also effectively obtained by the application of pulses, showing two well defined HRS and LRS states. Comparison with Au/LMO/Pt devices built on the same sample provided proof of the fundamental role of TiN as an active oxidizable electrode, and the successful combination of TiN/LMO for resistive switching applications.

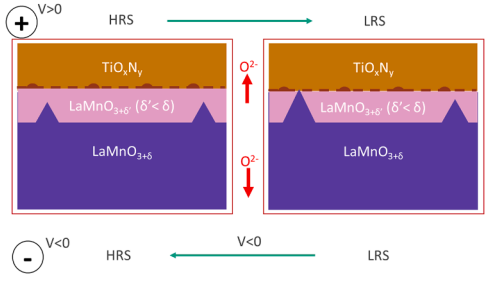

Fig. 7. Phenomenological resistive switching mechanism model based on oxygen-depleted ($LaMnO_{3+\delta}$) and oxygen-rich ($LaMnO_{3+\delta}$) LMO. On the left the oxygen depleted, high resistance LMO interlayer. On the right, after positive bias is applied, oxygen rich $LaMnO_{3+\delta}$ bridges through the oxygen depleted region leading to a low resistance state. The process is reversed when a negative bias is applied.

Declaration of Competing Interest

The authors declare that they have no known competing fianancial interests or personal relationship that could have appeared to influence the work reported in this paper.

Data availability

Data will be made available on request.

Acknowledgment

This work has been partially supported by the ANR funded projects “Alps Memories” (ANR-15-CE24-0018) and “Mangaswitch” (ANR-17-CE24-0038), and has also received funding from the European Union’s Horizon 2020 research and innovation program under the Marie Skłodowska-Curie Grant Agreement No. 746648 — PerovSiC (for D.P.). This research has benefited from characterization equipment of the Grenoble INP - CMTC platform supported by the Centre of Excellence of Multifunctional Architectured Materials "CEMAM" n°ANR-10-LABX-44-01 funded by the "Investments for the Future" Program. In addition, this work has been performed with the help of the “Plateforme

Technologique Amont" de Grenoble, with the financial support of the "Nanosciences aux limites de la Nanoélectronique" Fundation and CNRS Renatech network. Chevreul institute (FR 2638), the French ministry of research, the Région Hauts de France and FEDER are acknowledged for supporting and funding the surface analyses platform (ToF-SIMS). R.R-L. acknowledges the assistance of Dr. K.M. and Dr. B.R.G. for fruitful scientific discussions and for providing python codes and excel programs for data processing. The authors also acknowledge the use of the google SketchUp platform for 3D model building.

Supplementary materials

Supplementary material associated with this article can be found, in the online version, at doi:10.1016/j.mtelec.2023.100054.

References

[1] S. Spiga, Memristive Devices for Brain-Inspired Computing, Elsevier, 2020.
[2] S. Yu, H. Jiang, S. Huang, X. Peng, A. Lu, IEEE Circuits Syst. Mag. 21 (2021) 31–56.
[3] R. Waser, D. Ielmini, H. Akinaga, H. Shima, H.-S.P. Wong, J.J. Yang, S. Yu, Resist. Switch, Wiley-VCH Verlag GmbH & Co. KGaA, Weinheim, Germany, 2016, pp. 1–30.
[4] J.J. Yang, D.B. Strukov, D.R. Stewart, Nat. Nanotechnol. 8 (2013) 13–24.
[5] A. Sawa, Mater. Today 11 (2008) 28–36.
[6] F. El Kamel, P. Gonon, C. Vallée, V. Jousseaume, H. Grampeix, Appl. Phys. Lett. 98 (2011).
[7] Y.F. Chang, P.Y. Chen, B. Fowler, Y.T. Chen, F. Xue, Y. Wang, F. Zhou, J.C. Lee, J. Appl. Phys. 112 (2012), 123702.
[8] M. Lanza, A. Sebastian, W.D. Lu, M.Le Gallo, M.F. Chang, D. Akinwande, F. M. Puglisi, H.N. Alshareef, M. Liu, J.B. Roldan, Science 376 (2022) (80-.).
[9] R.S. Williams, Faraday Discuss 213 (2019) 579–587.
[10] R. Dittmann, S. Menzel, R. Waser, Adv. Phys. 70 (2021) 155–349.
[11] M. Janousch, G.I. Meijer, U. Staub, B. Delley, S.F. Karg, B.P. Andreasson, Adv. Mater. 19 (2007) 2232–2235.
[12] M. Asif, A. Kumar, Mater. Today Electron. 1 (2022), 100004.
[13] D. Panda, T.-Y. Tseng, Ferroelectrics 471 (2014) 23–64.
[14] S. Bagdzevicius, K. Maas, M. Boudard, M. Burriel, J. Electroceramics 39 (2017) 157–184.
[15] R. Waser, R. Dittmann, G. Staikov, K. Szot, Adv. Mater. 21 (2009) 2632–2663.
[16] D.B. Strukov, G.S. Snider, D.R. Stewart, R.S. Williams, Nature 453 (2008) 80–83.
[17] S. Majumder, K. Kumari, S.J. Ray, Mater. Lett. 302 (2021), 130339.
[18] W. Wu, H. Wu, B. Gao, N. Deng, S. Yu, H. Qian, IEEE Electron Device Lett 38 (2017) 1019–1022.
[19] S. Yu, X. Guan, H.S.P. Wong, IEEE Trans. Electron Devices 59 (2012) 1183–1188.
[20] W. Zhang, B. Gao, J. Tang, X. Li, W. Wu, H. Qian, H. Wu, Phys. Status Solidi – Rapid Res. Lett. 13 (2019), 1900204.
[21] L. Yao, S. Inkinen, S. van Dijken, Nat. Commun. 8 (2017) 14544.
[22] J.C. Gonzalez-Rosillo, R. Ortega-Hernandez, J. Jareño-Cerulla, E. Miranda, J. Suñe, X. Granados, X. Obradors, A. Palau, T. Puig, J. Electroceramics 39 (2017) 185–196.
[23] Hyunjun Sim, Hyejung Choi, Dongsoo Lee, Man Chang, Dooho Choi, Yunik Son, Eun-Hong Lee, Wonjoo Kim, Yoondong Park, In-Kyeong Yoo, Hyunsang Hwang, in: IEEE Int. Devices Meet. 2005. IEDM Tech. Dig. 2005, 2005, pp. 758–761.
[24] H. Nili, S. Walia, S. Balendhran, D.B. Strukov, M. Bhaskaran, S. Sriram, Adv. Funct. Mater. 24 (2014) 6741–6750.
[25] H. Nili, S. Walia, A.E. Kandjani, R. Ramanathan, P. Gutruf, T. Ahmed, S. Balendhran, V. Bansal, D.B. Strukov, O. Kavehei, M. Bhaskaran, S. Sriram, Adv. Funct. Mater. 25 (2015) 3172–3182.
[26] T. Menke, P. Meuffels, R. Dittmann, K. Szot, R. Waser, J. Appl. Phys. 105 (2009), 066104.
[27] D. Cooper, C. Baeumer, N. Bernier, A. Marchewka, C. La Torre, R.E. Dunin-Borkowski, S. Menzel, R. Waser, R. Dittmann, Adv. Mater. 29 (2017), 1700212.
[28] X. Sun, G. Li, X. Zhang, L. Ding, W. Zhang, J. Phys. D. Appl. Phys. 44 (2011), 125404.
[29] X. Sun, G. Li, L. Chen, Z. Shi, W. Zhang, Nanoscale Res. Lett. 6 (2011) 1–8.
[30] Y. Wang, M. Kim, C. Lee, A.S. Chabungbam, J. Kim, J. Lee, H.S. Lee, Q. Shao, H. Sohn, H.H. Park, Appl. Mater. Today 26 (2022), 101395.
[31] W.R. Acevedo, D. Rubi, J. Lecourt, U. Lüders, F. Gomez-Marlasca, P. Granell, F. Golmar, P. Levy, Phys. Lett. A 380 (2016) 2870–2875.
[32] E. Navickas, T.M. Huber, Y. Chen, W. Hetaba, G. Holzlechner, G. Rupp, M. Stöger-Pollach, G. Friedbacher, H. Hutter, B. Yildiz, J. Fleig, Phys. Chem. Chem. Phys. 17 (2015) 7659–7669.
[33] M. Lanza, K. Zhang, M. Porti, M. Nafría, Z.Y. Shen, L.F. Liu, J.F. Kang, D. Gilmer, G. Bersuker, Appl. Phys. Lett. 100 (2012), 123508.
[34] Z. Xu, K. Jin, L. Gu, Y. Jin, C. Ge, C. Wang, H. Guo, H. Lu, R. Zhao, G. Yang, Small 8 (2012) 1279–1284.
[35] R. Rodriguez-Lamas, D. Pla, O. Chaix-Pluchery, B. Meunier, F. Wilhelm, A. Rogalev, L. Rapenne, X. Mescot, Q. Rafhay, H. Roussel, M. Boudard, C. Jiménez, M. Burriel, Beilstein J. Nanotechnol. 10 (2019) 389–398.
[36] B. Meunier, D. Pla, R. Rodriguez-Lamas, M. Boudard, O. Chaix-Pluchery, E. Martinez, N. Chevalier, C. Jiménez, M. Burriel, O. Renault, ACS Appl, Electron. Mater. 1 (2019) 675–683.
[37] B. Meunier, E. Martinez, R. Rodriguez-Lamas, D. Pla, M. Burriel, C. Jimenez, Y. Yamashita, O. Renault, ACS Appl, Electron. Mater. 3 (2021) 5555–5562.
[38] B. Meunier, E. Martinez, R. Rodriguez-Lamas, D. Pla, M. Burriel, M. Boudard, C. Jiménez, J.-P. Rueff, O. Renault, J. Appl. Phys. 126 (2019), 225302.
[39] S. Balatti, S. Larentis, D.C. Gilmer, D. Ielmini, Adv. Mater. 25 (2013) 1474–1478.
[40] W. Zhang, J.-Z. Kong, Z.-Y. Cao, A.-D. Li, L.-G. Wang, L. Zhu, X. Li, Y.-Q. Cao, D. Wu, Nanoscale Res. Lett. 12 (2017) 393.
[41] K. Baek, S. Park, J. Park, Y.-M. Kim, H. Hwang, S.H. Oh, Nanoscale 9 (2017) 582–593.
[42] I. Maity, A.K. Mukherjee, A.D. Thakur, Appl. Phys. A Mater. Sci. Process. 129 (2023) 1–7.
[43] F. Borgatti, C. Park, A. Herpers, F. Offi, R. Egoavil, Y. Yamashita, A. Yang, M. Kobata, K. Kobayashi, J. Verbeeck, G. Panaccione, R. Dittmann, Nanoscale 5 (2013) 3954.
[44] K. Tsubouchi, I. Ohkubo, H. Kumigashira, M. Oshima, Y. Matsumoto, K. Itaka, T. Ohnishi, M. Lippmaa, H. Koinuma, Adv. Mater. 19 (2007) 1711–1713.
[45] A. Climent-Font, F. Pászti, G. García, M.T. Fernández-Jiménez, F. Agulló, Nucl. Instruments Methods Phys. Res. Sect. B Beam Interact. with Mater. Atoms (2004) 400–404. Elsevier.
[46] M. Mayer, SIMNRA User's Guide, (1997).
[47] M.N. Iliev, M.V Abrashev, J. Raman Spectrosc. 32 (2001) 805–811.
[48] Y. Takada, N. Okamoto, T. Saito, 3 (2015) 163–166.
[49] S. Farsinezhad, H. Sharma, K. Shankar, Phys. Chem. Chem. Phys. 17 (2015) 29723–29733.
[50] C. Ritter, M.R. Ibarra, J.M. De Teresa, P.A. Algarabel, C. Marquina, J. Blasco, J. García, S. Oseroff, S.-W. Cheong, Phys. Rev. B 56 (1997) 8902–8911.
[51] D. Maldonado, S. Aldana, M.B. González, F. Jiménez-Molinos, F. Campabadal, J. B. Roldán, Microelectron. Eng. 265 (2022), 111876.
[52] D. Maldonado, F. Aguirre, G. González-Cordero, A.M. Roldán, M.B. González, F. Jiménez-Molinos, F. Campabadal, E. Miranda, J.B. Roldán, J. Appl. Phys. 130 (2021), 054503.
[53] A.F. Zurhelle, W. Stehling, R. Waser, R.A. De Souza, S. Menzel, Adv. Mater. Interfaces 9 (2022), 2101257.
[54] J.J. Yang, J.P. Strachan, F. Miao, M.X. Zhang, M.D. Pickett, W. Yi, D.A.A. Ohlberg, G. Medeiros-Ribeiro, R.S. Williams, Appl. Phys. A Mater. Sci. Process. 102 (2011) 785–789.
[55] A. Herpers, C. Lenser, C. Park, F. Offi, F. Borgatti, G. Panaccione, S. Menzel, R. Waser, R. Dittmann, Adv. Mater. 26 (2014) 2730–2735.
[56] J.-S. Zhou, J.B. Goodenough, Phys. Rev. B 60 (1999) R15002–R15004.
[57] B. Arndt, F. Borgatti, F. Offi, M. Phillips, P. Parreira, T. Meiners, S. Menzel, K. Skaja, G. Panaccione, D.A. MacLaren, R. Waser, R. Dittmann, Adv. Funct. Mater. 27 (2017), 1702282.
[58] M. Lanza, G. Molas, I. Naveh, Nat. Electron. 64 (6) (2023) 260–263, 2023.